Phase-stepped ESPI and Moiré Interferometry for Measuring Stress-intensity Factor and *J* Integral

by A.J. Moore and J.R. Tyrer

ABSTRACT—Electronic-speckle-pattern interferometry and moiré interferometry have been used to calculate K_I and J for compact tension specimens. Automated-fringe-pattern analysis enables the full-field of data to be used with the minimum of operator intervention. Measurements are shown to be accurate to within 10 percent. The J-measurement procedure employed could form the basis of an automatic-fault detection system.

KEY WORDS—fracture mechanics, interferometry: electronic recording, moiré interferometry.

Introduction

The opening-mode stress-intensity factor and J integral are two parameters commonly used to describe the stress concentration at a crack tip. Optical techniques have been applied to measure K_I and J, either to determine the severity of cracks in a structure or to verify some aspect of fracture-mechanics theory. Those techniques which measure surface displacement principally include holographic interferometry,[1] moiré interferometry[2] and speckle photography.[3] Electronic-speckle-pattern interferometry[4] (ESPI) is less sensitive to environmental disturbances than holographic interferometry, does not require the application of a surface grating (moiré interferometry) and is not a point-wise measurement technique like speckle photography. Despite this, ESPI has previously been used only to detect the location of defects via local increases of fringe density or discontinuities in the fringe pattern.[5] Very little quantitative analysis of the interferograms has been undertaken, mainly because manual interpretation of the fringe patterns is laborious. Recently, automatic extraction of the displacement and strain distribution from ESPI fringe patterns recorded for a centrally notched plate was reported.[6] In this paper, it is demonstrated how ESPI can be used to measure K_I and J from such displacement and strain measurements. The emphasis is on automated-fringe-pattern analysis to take advantage of the full-field nature of ESPI measurements. Moiré interferometry has been used to validate the results obtained with ESPI. The same automated-fringe-analysis procedures have been used for the moiré-interferometry tests; the authors believe this also to be the first automated evaluation of fracture-mechanics parameters with moiré interferometry.

Three HS30TF aluminium-alloy compact-tension (CT) specimens were tested, Fig. 1. The specimens were statically loaded in a rigid hydraulic tensiometer. The tensiometer was clamped to the optics table, and hydraulic pressure applied remotely with a dead-weight tester. The specimen dimensions were calculated in proportion to the loading pin separation of the tensiometer. A maximum specimen thickness, B, of 6.35 mm could be accommodated by the tensiometer, insufficient to ensure plane-strain conditions. This is acceptable because all testing remained in the linear-elastic regime, and the value of K_I at the onset of brittle (plane-strain) fracture, K_{Ic}, was not to be determined. In order to exclude all plasticity effects, ≈4-mm notches of width 0.2 mm were introduced by electro-discharge machining (EDM) rather than fatigue cracking the specimens. This is analogous to the use of a slitting saw in photoelasticity; although crack acuteness is important at the fracture event, notches of width 1.2 mm are acceptable to accurately determine the geometrical shape factor,[7] Y, and hence K_I. Thus for $a/W > 0.35$, K_I values will be given by[8]

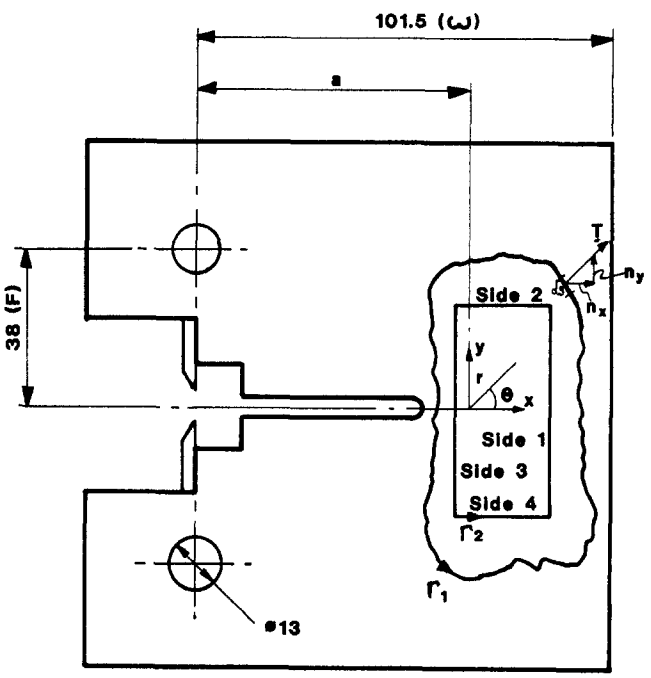

Fig. 1—Compact tension specimen (dimensions in mm)

A.J. Moore is Investigador Titular, Centro de Investigaciones en Optica A.C., Apdo. Postal I-948, Leon, Guanajuato, CP 37000, Mexico. J.R. Tyrer (SEM Member) is Senior Lecturer, Department of Mechanical Engineering, Loughborough University of Technology, Loughborough, Leics, LE11 3TU, United Kingdom.

Original manuscript submitted: February 7, 1994. Final manuscript received: November 29, 1994.

$$K_I = \frac{P}{BW^{1/2}} Y \quad (1)$$

where

$$Y = \frac{(2 + a/W)}{(1 - a/W)^{3/2}} \times [0.886 + 4.64(a/W) - 13.32(a/W)^2 + 14.72(a/W)^3 - 5.6(a/W)^4]$$

P is the applied load, and a and W are shown in Fig. 1. The a/W ratios for the three specimens tested (including EDM notch) were 0.56, 0.66 and 0.75. These specimens were denoted CT1, CT2 and CT3 respectively. The corresponding Y values from eq (1) are 11.74, 17.83 and 30.04.

Optical Techniques and Fringe Analysis

Three-dimensional deformation measurement with ESPI can be achieved by combining the displacements measured along three mutually perpendicular sensitivity vectors. These vectors are determined by the optical configuration of the interferometer, and are generally taken to be out-of-plane (perpendicular to the page in Fig. 1) and horizontal and vertical in-plane (parallel to the x and y axes respectively). However, measuring displacements ahead of the EDM notch in the CT specimens is essentially a two-dimensional problem, and the out-of-plane displacement component need not be measured. The illumination configuration required for in-plane sensitive ESPI is shown schematically in Fig. 2. Mutually coherent laser beams I_A and I_B lie in the xz plane and are incident on the test surface at equal angles, θ, to the x axis. Lens, L, forms a speckled image of the test surface along the z axis to camera 2. [Camera 1, the beamsplitter (PBS) and the beam pair I_C, I_D are not currently being considered.] The image of the undeformed test surface is stored in electronic memory and subtracted at the video frame-rate from subsequent live images of the deforming surface. A speckled cosinusoidal fringe pattern is formed, mapping contours of constant

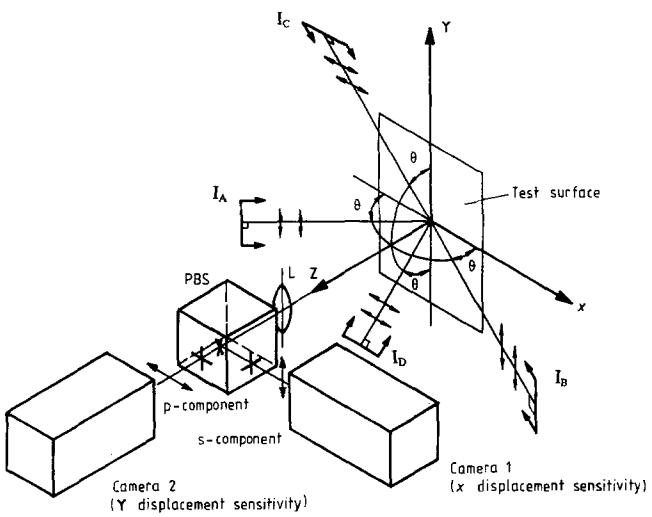

Fig. 2—Arrangement for interferometer distinguishing horizontal and vertical in-plane interferograms by polarization vector

phase difference between wavefronts I_A and I_B, for example Figs. 3(a). This phase difference can be related to surface displacement in the direction of the sensitivity vector. The sensitivity vector for this arrangement lies along the x axis and the incremental surface displacement between fringe peaks is given by the relationship

$$u = \frac{\lambda}{2\cos\theta} \quad (2)$$

where u is the surface displacement resolved parallel to the x axis and λ is the wavelength of light used. Rotating the illumination beam pair I_A, I_B to positions I_C, I_D in the yz plane (Fig. 2) gives sensitivity to displacements parallel to the y axis only, denoted by v.

The two dimensional in-plane displacement field can be measured by illuminating the test surface simultaneously with the beam pairs I_A, I_B and I_C, I_D, although the two speckle patterns must be optically distinguishable. A polarization discrimination method has been devised.[9] Beams I_A and I_B are both linearly polarized perpendicular to the plane of incidence, as suggested by the arrows in Fig. 2. This azimuth corresponds to one eigenaxis of the polarizing beamsplitter (PBS) and the image formed is reflected to camera 1. I_C and I_D are linearly polarized with orthogonal azimuths to I_A and I_B and hence parallel with the other eigenaxis of the beamsplitter. An image of the test surface illuminated by I_C and I_D is formed at camera 2. The speckle patterns associated with each illumination beam pair are therefore separated; correlation fringes produced from camera 1 correspond to displacements parallel to the x axis while camera 2 is sensitive to displacements parallel to the y axis. Notice that a single viewing lens is used to eliminate perspective differences between the images of the test surface. The success of the technique is dependent on the polarization state of the two speckle fields. The nature of the specimen surface contributes to the depolarization of the scattered wavefront, and consequently must be considered. Lightly abraded metal and silver spray-painted surfaces have been demonstrated to work effectively with this technique.[9] Cross-hatch abrading was used for the results presented in this paper. In the experimental system, beams I_A and I_B were expanded directly from a 0.5-W argon-ion laser (514 nm). I_C and I_D came from the same laser and were guided through highly birefringent optical fiber to the test surface. The output ends of the fibers were rotated to give polarization vectors orthogonal to I_A and I_B. Two identical CCD cameras were used to view the test area (25 mm × 25 mm) through a narrow-bandwidth polarizing beamsplitter cube. Spatial manipulation of camera 1 enabled the two views to be matched pixel for pixel. For all beams, $\theta = 45$ deg, yielding an ESPI sensitivity of 0.36 μm/fringe.

Moiré-interferometry results were recorded with the commercially available system Optecord, designed by Strathclyde University, Scotland.[10] The system consists of a single HeNe laser source which is divided into three 50-mm diameter beams which illuminate the measurement region along the x, y and 45-deg directions, similar to Fig. 2. Interference between pairs of the beams can be considered to provide stable reference gratings at 0, 45 and 90 deg to the x axis. A suitable crossed diffraction grating is bonded to the object under test. When positioned correctly within the measurement region, moiré interferometry

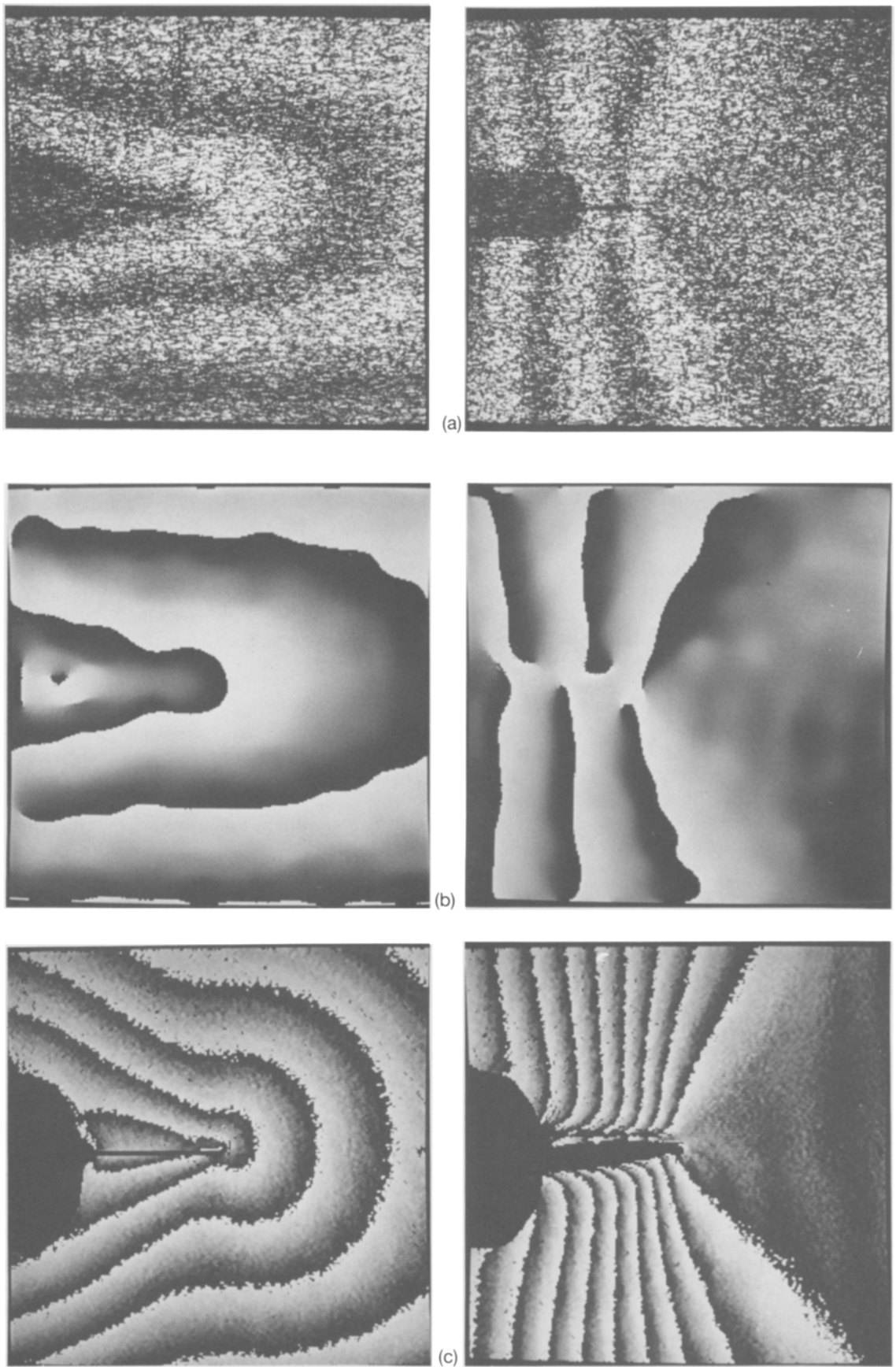

Fig. 3—Typical results. (a) ESPI fringes; (b) ESPI phase map; (c) moiré-interferometry phase map

fringes corresponding to in-plane displacements in the x, y and 45-deg directions are formed between the bonded grating and the selected reference grating. For these tests, the grating frequency was 950 lines/mm, yielding a moiré-interferometry sensitivity of 1.05 μm/fringe. Details of grating replication are given in the Optecord instruction manual.[10] The process involves casting a cross-diffraction grating in epoxy resin to the specimen surface; the mold is a silicone rubber replica made from a master grating. To enable reliable grating replication close to the notch tip, the notch was plugged with plasticine. Initial tests with the epoxy-resin grating were found to be unrepeatable on unloading and reloading the specimens. This was attributed to the brittle epoxy pulling away from the specimen surface in the region of the notch. Thus silicone rubber gratings, including the dye normally used in the epoxy resin, were used for the experiments reported here. An extra replication process is required: master grating to silicone rubber replica; silicone replica to epoxy resin replica; epoxy replica to silicone rubber grating cast on the specimen surface. Consequently the final grating was generally not of such good quality as that cast in epoxy. Measurements with 0 and 90-deg sensitivities (i.e., horizontal and vertical in-plane) are required to define the two-dimensional displacement field. Switching between illumination geometries (i.e., reference gratings) enabled horizontal and vertical displacements to be recorded sequentially. If desired, simultaneous recording along the two sensitivity vectors could be achieved using polarization discrimination as described above.

The fringe analysis[6] implemented to automatically determine displacement and strain from the recorded fringe patterns is beyond the scope of this paper, but will be described briefly. ESPI and moiré-interferometry fringe patterns reveal the magnitude of displacement, but not its direction along the sensitivity vector. This is because the optical-phase difference introduced between the interfering wavefronts due to deformation is displayed indirectly by the formation of fringes. To extract the phase difference a translating mirror may be placed in one beam of the interferometer.[6] Three fringe patterns are digitized to an image processor; precise control of the translating mirror enables discrete $2\pi/3$ radian phase steps to be introduced in one beam of the interferometer between recordings. The three intensities recorded at corresponding pixels in the three images, I_0, $I_{2\pi/3}$ and $I_{4\pi/3}$, are combined to give the optical phase, ϕ, at that position in the image.

$$\phi = \tan^{-1} \frac{I_{2\pi/3} - I_{4\pi/3}}{2I_0 - I_{2\pi/3} - I_{4\pi/3}} \quad \text{(modulo } 2\pi\text{)} \qquad (3)$$

Typical ESPI and moiré-interferometry phase results are shown in Figs. 3(b) and 3(c) for loads of 99N and 990N respectively. Phase values in the range 0 to 2π radians have been linearly scaled from 0 to 255 grey-levels for display. Discontinuities in the grey-scale occur due to the asymptotic nature of the arctangent function: it is the sign of these discontinuities that determines the direction of surface displacement and enables automated computer analysis of the interferogram. By adding or subtracting a 2π offset every time a discontinuity is encountered (a process termed phase-unwrapping) the displacement over the entire surface can be deduced by the computer. Finally, it is necessary to determine surface strain as the rate of change of in-plane displacement with respect to the x and y axes.[6] Each pixel is considered the center of a 25- × 25-pixel neighborhood, and a plane surface fitted to the displacement data in this region. The gradient of this plane parallel to the x and y axes yields the components of surface strain via

$$\varepsilon_{xx} = \frac{\partial u}{\partial x} \qquad \varepsilon_{yy} = \frac{\partial v}{\partial y}$$

$$\gamma_{xy} = \frac{\partial u}{\partial y} + \frac{\partial v}{\partial x} \qquad (4)$$

Phase-stepped ESPI was performed with a Kontron pipeline image processor, hosted by a DEC MicroVax. Images digitized by the Kontron (256 × 256 pixels with 8-bit resolution) may be accessed by the host computer for specific image-processing applications implemented in Fortran (for example calculating phase, unwrapping, calculating strain, calculating K_I and J). Phase-stepped moiré interferometry was performed with an Imaging Technology VG100 board (again 256 × 256 × 8 bits). Phase maps, for example Figs. 3(c), were transferred to the MicroVax for all subsequent analysis. Notice that the moiré-interferometry image becomes elongated in the vertical direction: the VG100 board uses rectangular pixels whereas the Kontron uses square pixels.

Experimental Method

For each specimen, 248N was applied to prestress the loading fixtures. ESPI measurements of displacement parallel to the x axis (u) and y axis (v), i.e., horizontal and vertical in-plane, were made at four equal load increments above this initial load. Eight phase maps were recorded for each specimen: u and v at each of the four loads. Between each load increment the electronic subtraction electronics were re-referenced. Consequently the phase maps measure the incremental displacement between successive loads. The displacement at the load line was monitored with a clip-gage mounted between knife edges, which were screwed to the CT specimens. Calibration proved the clip-gage to be linear over the range 0 to 0.7 mm, with resolution of 0.4 μm and an accuracy of approximately ±2 percent. Load line displacements were used to calculate strain-energy release rate (see 'Results and Discussion' below). Table 1 shows the loads applied to each of the three specimens (in addition to the initial prestress value) and the recorded displacement at the load line. Moiré-interferometry results were recorded for the same three CT specimens

TABLE 1—APPLIED LOADS AND LOAD LINE DISPLACEMENTS (LLD) FOR ESPI TESTS

	Specimen					
	CT1 (a/W = 0.56)		CT2 (a/W = 0.66)		CT3 (a/W = 0.75)	
Measurement Number	Load (N)	LLD (μm)	Load (N)	LLD (μm)	Load (N)	LLD (μm)
1	99	10.9	74	16.3	25	11.7
2	198	22.1	149	32.6	50	21.4
3	297	36.1	223	47.0	74	33.0
4	396	48.1	297	61.3	99	43.5

with the silicone rubber gratings bonded to the rear surface. For each specimen, an upper load limit was determined at which the unwrapping routine repeatedly failed for the v data due to the high fringe density. Phase maps were then recorded at four loads evenly distributed between the preload and the unwrapping-determined load limit. The load increments in addition to the prestress load are shown in Table 2, along with the recorded displacement at the load-line. Thus eight data files were transferred to the MicroVax for each specimen.

K_I Evaluation from Displacement Measurements

A least-squares solution originally proposed by Barker *et al.*[11] was used to calculate K_I from the u and v displacement measurements. This is based on a multi-parameter description of the displacement field surrounding the crack tip due to Sanford.[12]

$$Eu = \sum_{j=0}^{N} C_{2j} \frac{r^{j+1/2}}{j+1/2} [(1-\nu)\cos(j+1/2)\theta - (1+\nu)(j+1/2)\sin\theta\sin(j-1/2)\theta] + \sum_{j=0}^{N} C_{2j+1} \frac{r^{j+1}}{j+1} [2\cos(j+1)\theta - (1+\nu)(j+1)\sin\theta\sin j\theta] \quad (5a)$$

$$Ev = \sum_{j=0}^{N} C_{2j} \frac{r^{j+1/2}}{j+1/2} [2\sin(j+1/2)\theta - (1+\nu)(j+1/2)\sin\theta\cos(j-1/2)\theta] + \sum_{j=0}^{N} C_{2j+1} \frac{r^{j+1}}{j+1} [(1-\nu)\sin(j+1)\theta - (1+\nu)(j+1)\sin\theta\cos j\theta] \quad (5b)$$

E and v are Young's modulus and Poisson's ratio, respectively. Assume that n coefficients [C_0 to C_n, i.e., $j = 0$ to $n/2$ in eqs (5)] are required to adequately describe the displacement profile over the data-acquisition region. Both u and v are linear functions with respect to the unknown coefficients C_{2j}. If displacement measurements are made at m points ($m > n$) a set of over-determined linear equations is obtained, which may be expressed in matrix form by

TABLE 2—APPLIED LOADS AND LOAD LINE DISPLACEMENTS (LLD) FOR MOIRÉ INTERFEROMETRY TESTS

	Specimen					
	CT1 (a/W = 0.56)		CT2 (a/W = 0.66)		CT3 (a/W = 0.75)	
Measurement Number	Load (N)	LLD (μm)	Load (N)	LLD (μm)	Load (N)	LLD (μm)
1	495	60.6	495	103.7	248	116.9
2	990	124.2	743	161.5	446	219.3
3	1486	186.0	990	214.3	664	320.7
4	1981	254.7	1238	279.5	842	418.9

$$[Eu] = [S_u][C]$$
$$[Ev] = [S_v][C] \quad (6)$$

$[S_u]$ and $[S_v]$ are m (rows) × n (columns) matrices containing the constants in (r, θ) from eqs (5), and $[Eu]$ and $[Ev]$ are $m \times 1$ matrices of displacement at the m measurement points (r_i, θ_i). The $n \times 1$ elements of the coefficient matrix $[C]$ must be determined. Provided that $m > n$, the unknown coefficients can be determined in a least-squares sense, i.e., the problem reduces to determining the coefficients of the series which produce the best match to the displacement measurements at the selected points. K_I is related to the leading coefficient by

$$C_0 = \frac{K_I}{\sqrt{2\pi}} \quad (7)$$

Programs were written to collect (r_i, θ_i, u_i) and (r_i, θ_i, v_i) data sets from the unwrapped phase maps from a grid of points. Typically between 300 and 400 measurement points were used to minimize random phase errors. An eight-parameter solution [$j = 0$ to 4 in eqs (5)], with an additional two terms to allow for rigid-body motion,[11] was found to model the displacement field accurately.

J-evaluation from Displacement Measurements

The contour independent line integral J is defined by[13]

$$J = \int_\Gamma \left(Vdy - \boldsymbol{T}\frac{\partial \boldsymbol{u}}{\partial x}ds\right) \quad (8)$$

J may be evaluated for any contour enclosing the crack tip and traversed in an anti-clockwise direction, for example Γ_1 in Fig. 1. $\boldsymbol{u}$ is the displacement vector. V is the strain energy density, and may be calculated from the components of surface strain[14] (plane stress) by

$$V = \frac{E}{2(1-\nu^2)}(\varepsilon_{xx}^2 + \varepsilon_{yy}^2 + 2\nu\varepsilon_{xx}\varepsilon_{yy}) + \frac{\mu}{2}\gamma_{xy}^2 \quad (9)$$

μ is the shear modulus. $\boldsymbol{T} \equiv \sigma_{ij}n_j$ is the traction vector on Γ_1 according to an outward unit vector $\boldsymbol{n}$ (with direction cosines n_j) normal to the curve. For any contour

$$\boldsymbol{T}\frac{\partial \boldsymbol{u}}{\partial x} = \left(\sigma_{xx}\varepsilon_{xx} + \tau_{xy}\frac{\partial v}{\partial x}\right)n_x + \left(\sigma_{yy}\frac{\partial v}{\partial x} + \tau_{xy}\varepsilon_{xx}\right)n_y \quad (10)$$

The evaluation of this term is greatly simplified for a rectangular contour, Γ_2 in Fig. 1, because n_j take the values 0, −1 and 1. The components of stress $\boldsymbol{\sigma}_{ij}$ can be evaluated from strain measurements using Hooke's law[14] for plane-stress conditions,

$$\sigma_{xx} = \frac{E}{(1-\nu^2)}(\varepsilon_{xx} + \nu\varepsilon_{yy})$$
$$\sigma_{yy} = \frac{E}{(1-\nu^2)}(\varepsilon_{yy} + \nu\varepsilon_{xx}) \quad (11)$$
$$\tau_{xy} = \mu\gamma_{xy}$$

Provided that the contour passes through linear-elastic material,

$$J = \frac{K^2}{E} \tag{12}$$

The quantities V, σ_{ij}, ε_{xx} and $\partial v/\partial x$ were calculated for each pair of phase maps and written to a data file to avoid time-consuming recalculation. On defining two opposing corners of a rectangular contour, eq (8) was automatically evaluated from values read from the data file. Strain data were not available immediately adjacent to the notch line, due to the use of a 25- × 25-pixel window in calculating strain. Thus side 3 of any contour enclosing the notch tip will include a length for which no valid data are available. V and $T\partial \boldsymbol{u}/\partial x$ are smaller close to the free crack surface than at other points on the contour. The omission of a few data points makes very little difference to the overall contour integral.

Results and Discussion

K_I measurements for the three CT specimens are shown in Fig. 4. The graphs for ESPI, Fig. 4(a), and moiré interferometry, Fig. 4(b), both contain 48 measurement points: two (r_i, θ_i, u_i) and two (r_i, θ_i, v_i) data sets gathered at each of the four loads for three specimens. The experimentally determined K_I values (ordinate) were calculated from the leading coefficient, C_0, of the least-squares fit using eq (7). The theoretical K_I values (abscissa) were calculated from eq (1) using the loads given in Tables 1 and 2.

The subtraction electronics were re-referenced between each load increment for the ESPI measurements. Each phase map therefore measures the incremental displacement between successive loads; hence the increase in K_I between successive loads is calculated from each phase map. The pair of 'incremental' K_I measurements for each phase map is seen at the bottom of Fig. 4(a). K_I is linearly related to displacement. Consequently, the mean of each pair of incremental measurements has been added to give a 'cumulative' horizontal in-plane (HIP) and vertical in-plane (VIP) total for each specimen, Fig. 4(a). An alternative solution would be to sum successive displacement measurements before collecting the (r_i, θ_i, u_i) and (r_i, θ_i, v_i) data sets. Moiré interferometry measures this total (cumulative) displacement giving K_I at each load directly, Fig. 4(b). It is evident from both graphs that in some cases the solution calculated from vertical in-plane displacement data converges to a least-squares best-fit set of coefficients that does not give the leading term correctly. [CT3 VIP in Fig. 4(a), CT1, CT2, CT3 VIP in Fig. 4(b).] In fact, a negative K_I value was obtained at load 1 from the vertical in-plane moiré-interferometry data for CT2. Chona *et al.*[15] encountered this problem in photoelastic studies and proposed a sampled least-squares method for analysis of the data, to be used "whenever necessary." These erroneous solutions are generally consistent for both the data sets taken from each vertical in-plane phase map, and in some instances increase linearly with load [CT3 VIP in Fig. 4(a), CT1, CT2 VIP in Fig. 4(b).] Consequently it is not apparent from the vertical in-plane K_I values alone when recourse to the sampled least-squares solution is necessary, unless the result is wildly in error, e.g., negative. Rather than using a sampled least-squares solution, therefore, only experimental K_I values calculated from horizontal in-plane phase maps were used in the subsequent analysis.

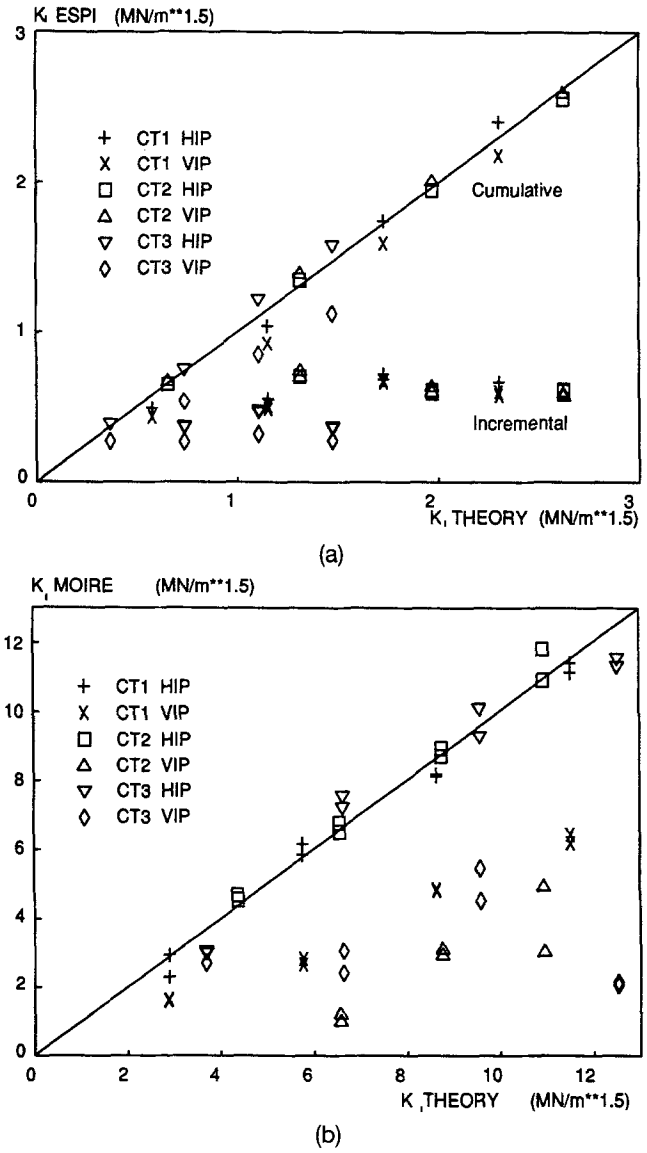

Fig. 4—K_I measurements for CT1, CT2 and CT3. (a) ESPI; (b) moiré interferometry

Deviations between theoretical and experimental K_I values arise due to residual speckle noise in the phase data: no systematic error is apparent for the horizontal in-plane values. The mean difference between two measurements taken from the same horizontal in-plane phase map is 0.01 $MN/m^{3/2}$ and 0.35 $MN/m^{3/2}$ for the ESPI and moiré-interferometry tests respectively. This corresponds to a signal-to-noise ratio of 36 dB and 30 dB over the respective measurement ranges of $\approx$0.7 $MN/m^{3/2}$ for ESPI and $\approx$11.7 $MN/m^{3/2}$ for moiré interferometry. All cumulative ESPI and moiré-interferometry results fall within $\pm$10 percent and $\pm$11 percent respectively of the theoretical values. Thus the accuracy of both techniques is comparable. Figures 4(a) and 4(b) are combined for a specimen CT2 in Fig.

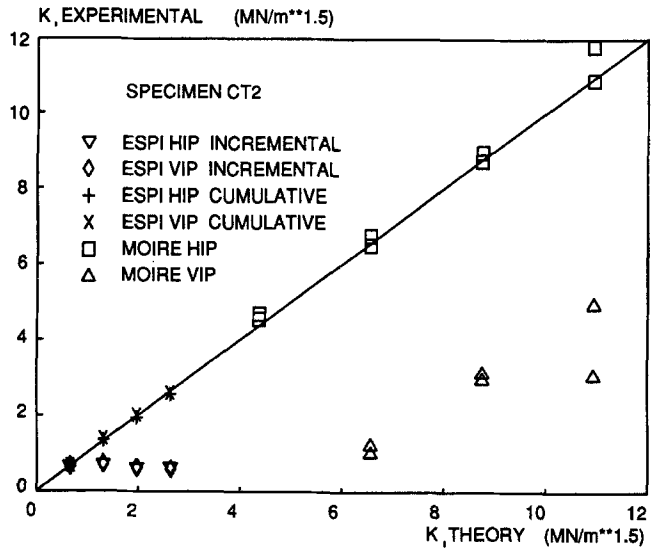

Fig. 5—Comparison of ESPI and moiré-interferometry K_1 measurements for CT2

5. This emphasizes the sensitivity of ESPI, although the measurement range is significantly less than for moiré interferometry. However, it is possible to calculate cumulative values with ESPI as demonstrated.

The J integral should be constant for any contour that encloses the notch tip, and zero otherwise. Noise in the measured strain data will cause J to vary with the contour chosen. In order to study the noise present in J measurements, the following test was performed. Referring to Fig. 1 showing the rectangular contour, sides 1, 2 and 4 were defined at the edge of available data. Side 3 was then traversed from the left-hand edge of the image to the right, one pixel at a time. J was calculated for each contour thus defined. The process was then repeated, but with sides 1, 2 and 3 at the image edges and side 4 traversed down the image. This test can be performed very quickly, because the required data are available at nearly all points in the image (i.e., full-field measurement, and J is evaluated automatically). Figure 6 shows the result of continuous variation in the position of side 3 for specimen CT1. ESPI measures the J increment between successive loads, Fig. 6(a), while moiré interferometry, Fig. 6(b), measures the cumulative J value. The x position of the notch tip is indicated by a vertical line in both graphs. When side 3 is positioned to the left of this line, the contour encloses the notch tip and J takes a positive, theoretically constant, value. The notch tip is not enclosed to the right of the line, and J falls theoretically to zero. Consider the J measurement for load 1 in Fig. 6(a). The x values at which local maxima and minima occur to the left of the notch tip have been denoted $x_{3,\max}$ and $x_{3,\min}$, respectively. Similarly, to the right of the notch tip, the maxima and minima are marked at $x_{1,\max}$ and $x_{1,\min}$. With the y positions of sides 2 and 4 given in the figure, maximum J occurs for side 3 at $x_{3,\max}$ and side 1 at $x_{1,\min}$. The minimum value will be given with sides 3 and 1 at $x_{3,\min}$ and $x_{1,\max}$, respectively. It is possible to determine the corresponding values $y_{2,\max}$, $y_{2,\min}$, $y_{4,\max}$ and $y_{4,\min}$ from the plot of J with continuous variation in side 4. From these x and y values, two final contours were

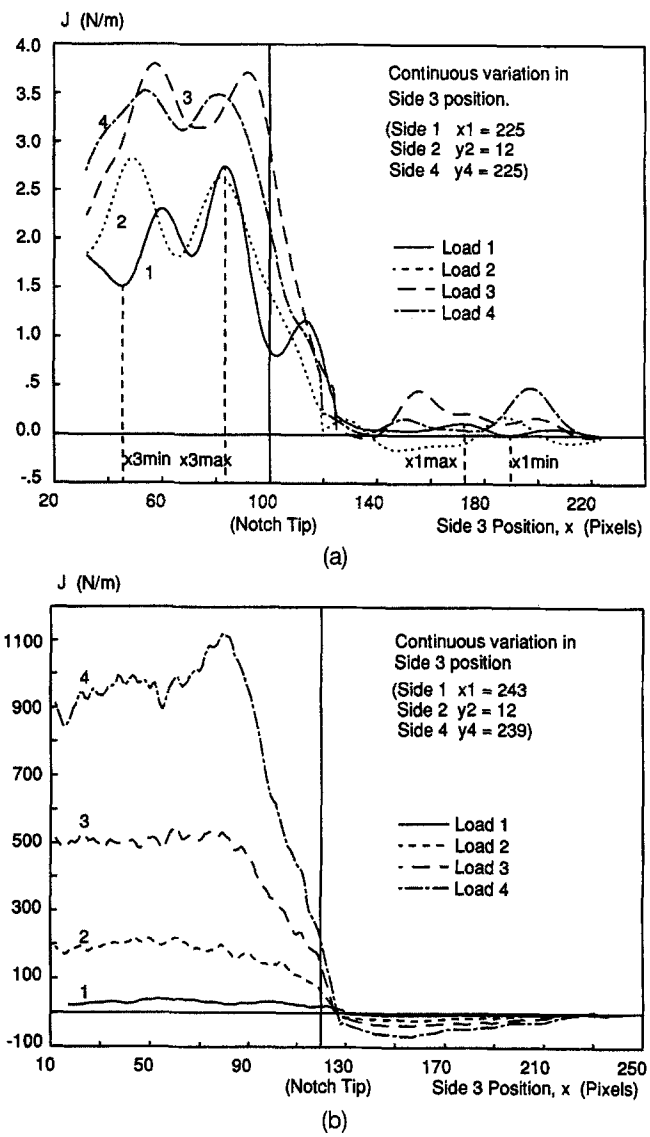

Fig. 6—J variation with contour for CT1. (a) ESPI; (b) moiré interferometry

constructed: $x_{1,\min}$, $y_{2,\min}$, $x_{3,\max}$, $y_{4,\max}$ for sides 1 through 4 respectively giving 'maximum' J, while $x_{1,\max}$, $y_{2,\max}$, $x_{3,\min}$, $y_{4,\min}$ gave a 'minimum.' Clearly not every possible J value has been calculated by this procedure, but the two contours give a reasonable approximation to the global maximum and minimum J values.

The range of J values calculated for each specimen at each load is shown by the error bars in Fig. 7. Incremental ESPI measurements are shown at the bottom of Fig. 7(a). To determine the cumulative J value, $J_{2,\text{cum}}$, from successive incremental measurements K_1, J_1 and K_2, J_2, a relationship of the form $J = cK^2$ was assumed (c = constant), eq (12). Then

$$J_{2,\text{cum}} = c(K_1 + K_2)^2 = J_1 + 2\sqrt{J_1 J_2} + J_2 \quad (13)$$

The mean value for each measurement has been marked. An uncertainty in any single J measurement of 33 percent is indicated. Due to the cyclic variation in J with contour

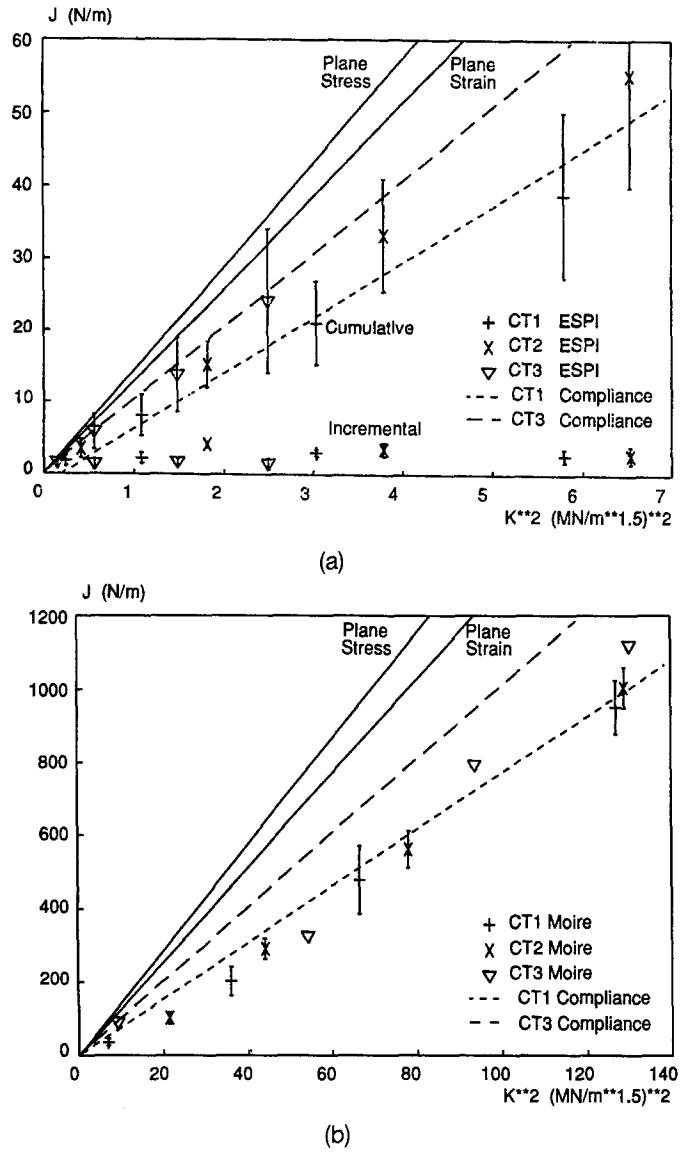

Fig. 7—J measurement for CT1, CT2 and CT3. (a) ESPI; (b) moiré interferometry

position, Fig. 6(a), this can be reduced by averaging several measurements. This cyclic variation is possible due to small errors in the size of the applied phase-step caused by environmental disturbances. The moiré-interferometry results for specimen CT1 are shown in Fig. 7(b). The uncertainty in a single J measurement is 18 percent. The noise in the moiré-interferometry J measurements appears random, Fig. 6(b). Consequently the uncertainty in J may also be reduced by averaging several measurements.

The expected relationships between J and K^2 under plane-stress, eq (12), and plane-strain conditions are plotted in Figs. 7(a) and 7(b). A variation is seen between these theoretical values and the experimental results. A possible explanation is the presence of the EDM notch rather than a true stress singularity. The J-evaluation routines were not in error, because tests on theoretical data sets gave the expected relationship. Secondly the moiré-interferometry measurements confirm the ESPI results. As an independent check, the values in Tables 1 and 2 were plotted on a graph of load against load point displacement. The compliance, C, of each specimen is defined as (1/gradient) of the load-displacement graph. These values of compliance may then be plotted against crack length, from which an estimate of $\partial C/\partial a$ was made for each specimen. Compliance testing was an early fracture-mechanics technique by which the strain-energy release rate,[16] G, was calculated.

$$G = \frac{P^2}{2B}\left(\frac{\partial C}{\partial a}\right) \tag{14}$$

For linear-elastic conditions,[13] $J \equiv G$. Figure 7 shows the best fit line to G values for CT1 and CT3, which bound the ESPI measurements. The mean ESPI measurements fall within 10 percent of the value calculated from the specimen compliance. Moiré-interferometry results also agree well with the compliance values. Finally cumulative ESPI and moiré-interferometry results are plotted on the same axes in Fig. 8. Again this highlights the sensitivity of ESPI and the substantially larger dynamic range of moiré-interferometry measurements.

Conclusions

It is demonstrated that ESPI may be successfully used to measure K_I with a signal-to-noise ratio of 36 dB over the approximate range of 0.7 MN/m$^{3/2}$. All cumulative ESPI results fall within ± 10 percent of the theoretical values. J values averaged over several contours agree to within 10 percent with compliance measurements. Averaging over several contours[2,3] is a procedure adopted with other optical techniques to measure J. All results are verified with phase-stepped moiré-interferometry measurements made from the same specimens: K_I values from moiré interferometry show a signal-to-noise ratio of 30 dB over the approximate measurement range of 11.7 MN/m$^{3/2}$; systematic errors in J of ± 18 percent have been recorded for $J < 1200$ N/m. Moiré-interferometry and ESPI results were in excellent agreement. This comparison highlights the sensitivity of ESPI, although the measurement range is significantly less than for moiré interferometry. However, it is possible to

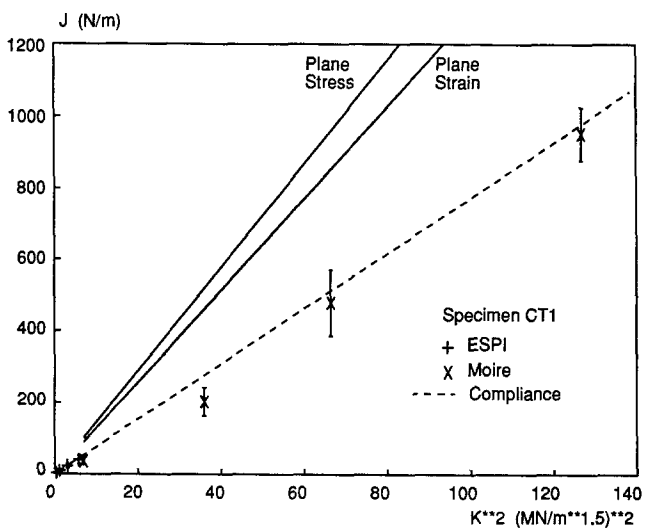

Fig. 8—Comparison of ESPI and moiré-interferometry J measurements for CT1

calculate cumulative values with ESPI as demonstrated. Both techniques have their niche. Moiré interferometry is useful for relatively large-scale deformation (e.g. plasticity) when coherent interferometric conditions would be lost for ESPI. However, moiré interferometry requires a reference phase grating to be bonded to the specimen surface, which must be relatively flat. ESPI can be used for objects of arbitrary surface profile without the need to apply a surface grating. Also, dynamic studies involving pulsed ESPI would be well suited to this sensitivity range: the pulse separation can be adjusted to vary the sensitivity further. Processing the displacement data takes approximately one minute for K_I and 10 minutes for J. Finally, the procedure for determining the range of J values, Fig. 6, could form the basis of an automatic fault-detection system.

Acknowledgments

This work was funded by the Science and Engineering Research Council, UK. The authors wish to thank John Brownell of Rolls Royce PLC, Derby for assistance in recording the moiré-interferometry results presented in the paper.

References

1. *Dudderar, T.D. and Gorman, H.J., "The Determination of Mode 1 Stress-intensity Factors by Holographic Interferometry,"* EXPERIMENTAL MECHANICS, **13** *(13), 145–149 (1973).*

2. *Marshall, S.J., Rixon, R.C., Caulfield, M.M. and MacKenzie, P.M., "The Application of Automatic Fringe Analysis in Fracture Mechanics," Optics and Lasers in Eng.,* **7,** *175–193 (1987).*

3. *Huntley, J.M. and Field, J.E., "Measurement of Crack Tip Displacement Field Using Laser Speckle Photography," Eng. Fract. Mech.,* **30** *(6), 779–790 (1988).*

4. *Jones, R. and Wykes C., Holographic and Speckle Interferometry, 2nd Ed., Cambridge Univ. Press, Cambridge, Chap. 4 (1988).*

5. *Holscher, C., Gulker, G., Hinsch, K., Kramer, A. and Neunaber, H., "The Investigation of Natural Stones Under Test-conditions by ESPI," Proc. Soc. of Photo-optical Instr. Eng., SPIE, Bellingham, WA,* **863,** *162–166 (1987).*

6. *Moore, A.J. and Tyrer, J.R., "Surface Strain Measurement with ESPI Applied to Fracture Mechanics," Proc. Hologram Interferometry and Speckle Metrology, 192–198, SEM (1990).*

7. *Kobayashi, A.S., "Photoelasticity Techniques," Experimental Techniques in Fracture Mechanics, ed. A.S. Kobayashi, Iowa State Press, 126–142 (1973).*

8. *E1290-89 Standard Test Method for Crack-tip Opening Displacement (CTOD) Fracture Toughness Measurement, Amer. Soc. Test. and Mat. (1989).*

9. *Moore, A.J. and Tyrer, J.R., "An Electronic Speckle Pattern Interferometer for Complete In-plane Displacement Measurement," Measurement Sci. and Tech.,* **1** *(10), 1024–1030 (1990).*

10. *Anon, "Optecord Live Fringe Interferometer: Instruction Manual," Strathclyde Univ.*

11. *Barker, D.B., Sanford, R.J. and Chona, R., "Determining K and Related Stress-field Parameters from Displacement Fields,"* EXPERIMENTAL MECHANICS, **25** *(12), 399–407 (1985).*

12. *Sanford, R.J., "A Critical Re-examination of the Westergaard Method for Solving Opening-mode Crack Problems," Mech. Res. Comm.,* **6** *(5), 289–294 (1979).*

13. *Rice, J.R. and Rosengren, G.F., "Plane Strain Deformation near a Crack Tip in a Power-law Hardening Material," J. Mech. and Physics of Solids, 16 1–12 (1968).*

14. *Timoshenko, S.P. and Goodier, J.N., Theory of Elasticity, 3rd Ed., McGraw-Hill (eqs 134 and 26, 27) (1970).*

15. *Chona, R., Irwin, G.R. and Sanford, R.J., "Influence of Specimen Size and Shape on the Singularity Dominated Zone," Special Tech. Publication 791, Amer. Soc. for Test. and Mat., 13–123 (1983).*

16. *Irwin, G.R. and Kies, J.A., "Critical Energy Rate Analysis of Fracture Strength," Welding J.,* **33** *(4), 193s–198s (1954).*